

Direct Observation of Unidirectional Density Wave and Band splitting in a Single-Domain Trilayer Nickelate $\text{Pr}_4\text{Ni}_3\text{O}_{10}$

Zhicheng Jiang,^{1,*} Enkang Zhang,^{2,3,*} Yuxin Wang,^{4,*} Zhengtai Liu,^{5,6,†} Jishan Liu,^{5,6} Runfeng Zhang,¹ Xinnuo Zhang,¹ Wenchuan Jing,⁶ Yu Huang,⁶ Qi Jiang,^{5,6} Mao Ye,^{5,6} Kun Jiang,^{7,‡} Jun Zhao,^{2,3,8,9,§} Dawei Shen,^{1,¶} and Donglai Feng^{10,**}

¹*National Synchrotron Radiation Laboratory and School of Nuclear Science and Technology, University of Science and Technology of China, Hefei, 230026, China*

²*State Key Laboratory of Surface Physics and Department of Physics, Fudan University, Shanghai, 200433, China*

³*Shanghai Research Center for Quantum Sciences, Shanghai, 201315, China*

⁴*Kavli Institute for Theoretical Sciences, University of Chinese Academy of Sciences, Beijing, 100190, China*

⁵*Shanghai Synchrotron Radiation Facility, Shanghai Advanced Research Institute, Chinese Academy of Sciences, Shanghai 201210, China*

⁶*Shanghai Institute of Microsystem and Information Technology, Chinese Academy of Sciences, Shanghai 200050, China*

⁷*Institute of Physics, Chinese Academy of Sciences,*

Beijing National Laboratory for Condensed Matter Physics, Beijing, 100190, China

⁸*Institute of Nanoelectronics and Quantum Computing, Fudan University, Shanghai, 200433, China*

⁹*Hefei National Laboratory, Hefei, 230088, China*

¹⁰*New Cornerstone Science Laboratory, University of Science and Technology of China, Hefei, 230026, China*

Unraveling the interplay between density-wave (DW) instabilities and multi-orbital physics is critical for understanding superconductivity in Ruddlesden-Popper nickelates, yet intrinsic electronic features have been persistently obscured by material inhomogeneity and thus the multi-domain averaging effect. Here, we employ micro-focused angle-resolved photoemission spectroscopy (μ -ARPES) on single-domain $\text{Pr}_4\text{Ni}_3\text{O}_{10}$ to disentangle the complex hierarchy of intrinsic and back-folded bands, explicitly identifying the electronic states driving the DW phase transition. We provide decisive spectroscopic evidence that the low-energy reconstruction is governed by inter-orbital nesting between the α and β bands. Specifically, we resolve a orbital-dependent gap of ~ 44 meV on the α pocket, a value quantitatively consistent with prior measurements, unifying previously conflicting experimental reports regarding the locus and magnitude of the DW gap. Furthermore, we reveal strong orbital-selective mass renormalization in the d_{z^2} states and successfully resolve the long-sought intrinsic trilayer β -band splitting, establishing a critical lower bound for the outer-layer hopping. These results define a coherent microscopic fingerprint for the trilayer nickelates, identifying the specific nesting channels and correlation effects that underpin the phase diagram.

INTRODUCTION

A hallmark of unconventional superconductivity, as exemplified by cuprates and iron-based superconductors, is its close proximity and competition with spin/charge density-wave (DW) orders [1, 2]. These DW instabilities are believed to play a critical role in shaping the superconducting ground state, potentially even driving the pairing mechanism itself [3]. Recently, the discovery of high temperature superconductivity in pressurized Ruddlesden-Popper (RP) nickelates, most notably the bilayer $\text{La}_3\text{Ni}_2\text{O}_7$ and trilayer $\text{La}_4\text{Ni}_3\text{O}_{10}$, has ignited intense interest in exploring analogs in nickel-based systems [4–11]. Similar to their iron-based counterpart, these layered nickelates exhibit robust DW transitions at ambient pressure, which are suppressed under applied pressure, coinciding with the emergence of superconductivity [12–14]. Deciphering the microscopic electronic structure underpinning the DW phases is therefore crucial to understanding the mechanism of superconductivity in nickelates.

However, experimentally accessing this electronic

structure has proven exceptionally difficult. The intrinsic material complexities, including oxygen non-stoichiometry, structural inhomogeneity [15–18], and the coexistence of multiple DW domains [19, 20], severely hinder precise spectroscopic characterization. Consequently, while scanning tunneling microscopy (STM) and optical spectroscopy have detected local charge modulations and hints of DW gap formation [14, 21], angle-resolved photoemission spectroscopy (ARPES) has yet to unambiguously identify DW-related electronic features. In $\text{La}_3\text{Ni}_2\text{O}_7$, for instance, clear DW gaps on the Fermi surface remain elusive [22]. The situation is even more perplexing in $\text{La}_4\text{Ni}_3\text{O}_{10}$, where conflicting observations have emerged: one study identified an SDW gap on the flat, hole-like γ pocket [23], whereas a separate study observed the gap on the electron-like α pocket, reporting a size much smaller than that discovered in STM and optical spectroscopy [14, 22]. This experimental ambiguity stands in stark contrast to theoretical simulations, which identify Fermi-surface nesting as a key driver for DW instability, yet direct verification of the expected band folding and gap opening remains elusive [24]. Compound-

ing this issue, previous ARPES measurements revealed surprisingly similar Fermi surfaces for both trilayer and bilayer nickelates, contradicting the distinct topologies predicted by first-principles calculations [25–28].

The recently discovered $\text{Pr}_4\text{Ni}_3\text{O}_{10}$ offers a superior platform due to its high crystalline quality and structural uniformity [10]. In this work, we employ micro-focused ARPES (μ -ARPES) to selectively probe a single structural/electronic domain of $\text{Pr}_4\text{Ni}_3\text{O}_{10}$, effectively circumventing the spectral blurring arising from domain superposition. This domain-resolved approach allows us to directly observe the intrinsic trilayer-splitting of bands, alongside distinct back-folded bands originating from structural distortions and intertwined density-wave orders. By disentangling these complex features in momentum space, we recognize the gap opening related to the SDW. Our results successfully clarify the long-standing ambiguities in the field, providing compelling evidence that the gap opening is driven by a unidirectional, incommensurate SDW order.

CRYSTAL STRUCTURE

Single crystals of $\text{Pr}_4\text{Ni}_3\text{O}_{10}$ adopt the $n = 3$ member of the RP structure series, characterized by perovskite blocks of three NiO_6 octahedra layers separated by rock-salt layers [Fig. 1(a)]. Analogous to its isostructural counterpart $\text{La}_4\text{Ni}_3\text{O}_{10}$, collective tilting and rotation of these NiO_6 octahedra in $\text{Pr}_4\text{Ni}_3\text{O}_{10}$ at ambient pressure drive a distortion from the tetragonal structure, resulting in an in-plane $\sqrt{2} \times \sqrt{2}$ superlattice reconstruction. Fig. 1(b) presents a top-down schematic of this structure with Pr atoms omitted for clarity, where the original unit cell is marked by a dashed box and the superlattice cell by a solid frame. Correspondingly, X-ray diffraction measurements confirm that $\text{Pr}_4\text{Ni}_3\text{O}_{10}$ crystallizes in the monoclinic space group $\text{P}2_1/\text{c}$, with lattice parameters $a = 5.377 \text{ \AA}$ and $b = 5.465 \text{ \AA}$, respectively [10].

The trilayer structure results in two crystallographically inequivalent NiO_6 planes, corresponding to the inner and outer layers. The DFT calculations predict that this structural inequivalence lifts the degeneracy of the β bands, which are primarily of $\text{Ni } 3d_{x^2-y^2}$ character, leading to a sizable band splitting as schematically illustrated in Fig. 1(c). The resistivity curve measured at ambient pressure [Fig. 1(d)] exhibits a distinct anomaly at $T_{DW} \approx 157 \text{ K}$, marking a transition into a state with coexisting spin- and charge-density-wave (SDW/CDW) order.

Previous X-ray and neutron scattering results [24, 29] have established that these density waves propagate along a unidirectional diagonal direction of the Ni-square lattice ($\mathbf{q}^* \parallel a/b$), with $\mathbf{q}_{sdw} = 0.61\mathbf{q}^*$ and $\mathbf{q}_{cdw} = 0.78\mathbf{q}^*$, as shown in Fig. 1(e). While recent local probes, such as STM on the sibling compound $\text{La}_4\text{Ni}_3\text{O}_{10}$ [21], reported an anisotropic CDW wave vector, this anisotropy

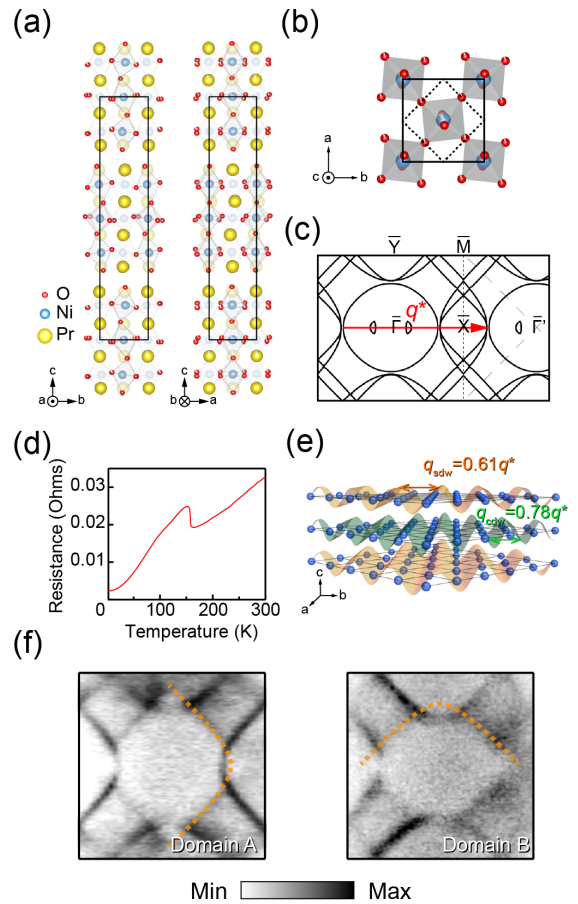


FIG. 1. (a) Side view of the crystal structure of $\text{Pr}_4\text{Ni}_3\text{O}_{10}$, dark frame indicates the unit cell (consisting of two $\text{Pr}_4\text{Ni}_3\text{O}_{10}$ formula units); (b) Top view of the crystal structure with a two-dimensional lattice of O and Ni atoms. The dash dark line frame represent the original unit cell without considering the tilted Ni-O octahedra and the solid line frame represents the real structural unit cell by considering the tilting of the Ni-O octahedra; (c) Calculated Fermi surface of $\text{Pr}_4\text{Ni}_3\text{O}_{10}$ obtained from the DFT calculations, appended red arrow represent the scattering \mathbf{q}^* is the unit scattering vector. To note, the anisotropy lattice parameter generate 0.01 \AA^{-1} difference on k_x/k_y direction of the Brillouin zone. Therefore the magnitude of unit scattering vector \mathbf{q}^* can be denoted as $q^* = \frac{2\pi}{(a+b)/2}$. (d) In-plane resistivity (ρ_{ab}) of $\text{Pr}_4\text{Ni}_3\text{O}_{10}$; (e) Schematic SDW and CDW alien with Ni lattice model, the SDW/CDW propagates unidirectionally along the a/b -axis of the crystal lattice. (f) The two domains with orthogonal electronic structures measured in the $\text{Pr}_4\text{Ni}_3\text{O}_{10}$.

has proven elusive to spatially-averaged techniques like conventional photoemission and X-ray scattering [23, 30]. This failure is widely attributed to spatial averaging over multiple coexisting crystalline or electronic domains.

Our μ -ARPES results, acquired from a single-domain region using a $\sim 15 \times 15 \mu\text{m}^2$ beam spot, are displayed in Fig. 1(f). The measured Fermi surface maps deviate significantly from previous ARPES reports [23, 31]. Specifically, near the Brillouin zone center, we observed a prominent “arc-like” feature (marked by orange dashed

lines). Although this feature was previously attributed to the α electron pocket, this assignment is inconsistent with the relatively isotropic α -band from DFT calculations [23]. Instead, our data in Fig. 1(f) clearly show that this feature intersects and hybridizes with the β band. In the following sections, we will disentangle and analyze these band characteristics in detail.

INTRINSIC ELECTRONIC STRUCTURE AND ORBITAL-SELECTIVE CORRELATIONS

Fig. 2(a) presents a photon-energy-dependent map of the band structure in an intentionally selected single domain along the $\bar{\Gamma} - \bar{X}$ high-symmetry direction. All primary electronic bands can be observed along this cut, with the α/β bands located near the Brillouin zone center ($k_{\parallel}=0$) and the higher-intensity γ band situated around the \bar{X} points. The α/β bands exhibit negligible dispersion as a function of photon energy, indicating their two-dimensional character. In contrast, the γ band shows pronounced warping, which signifies a substantial dispersion along the out-of-plane momentum direction (k_z). These findings are consistent with the primary orbital characters of the bands: the α/β bands derive mainly from the in-plane Ni $3d_{x^2-y^2}$ orbitals, conferring their 2D nature, while the γ band originates from the out-of-plane Ni $3d_{z^2}$ orbital, giving rise to its substantial k_z dispersion.

A photon energy of 75 eV was then chosen for detailed measurements, as it provides the sharpest spectral features, as well as facilitating a direct comparison with previous ARPES studies on RP nickelates [22, 23, 31, 32]. Fig. 2(b) displays the Fermi surface measured at this photon energy, which clearly resolves the α/β Fermi pockets (marked by red arrows). Additionally, replica bands from octahedral distortion, denoted as β_{oct} , can be also clearly resolved. This feature likely arises from the band folding induced by the superlattice potential of the tilted NiO_6 octahedra. We then quantitatively extracted the Fermi momenta for all observed pockets through both energy distribution curves (EDC) and momentum distribution curves (MDC) analysis, which are summarized as the contours in Fig. 2(c). This Fermi surface is highly consistent with that of $\text{La}_4\text{Ni}_3\text{O}_{10}$ [23, 31].

Fig. 2(d) and 2(e) present the detailed band dispersions along the high-symmetry directions indicated in Fig. 2(c). By comparing these data with our orbital-projected first-principles calculations [Fig. 2(f)], we could unambiguously assign the orbital characters of the observed bands. The α and β bands possess predominantly $d_{x^2-y^2}$ character, while the γ band is primarily of d_{z^2} character. The γ band top is located at ≈ 30 meV below E_F , similar to that reported for $\text{La}_3\text{Ni}_2\text{O}_7$ [22]. However, a significant discrepancy emerges: the experimental bandwidths are substantially compressed relative to

the DFT calculations. This indicates strong carrier mass renormalization (*i.e.*, self-energy effects) driven by electron correlations in $\text{Pr}_4\text{Ni}_3\text{O}_{10}$.

To quantify this, we extracted the mass renormalization factor (m^*/m_b) for each band. The $d_{x^2-y^2}$ -derived bands show moderate renormalization: $m^*/m_b \approx 5$ for the α band and $m^*/m_b \approx 2.9\text{--}3.0$ for the β band. Strikingly, the d_{z^2} -derived γ band is renormalized by a factor of $m^*/m_b \approx 16.7$. This enormous value, while vastly exceeding that of the $d_{x^2-y^2}$ bands, is consistent with the physics of related nickelates. For instance, in bilayer $\text{La}_3\text{Ni}_2\text{O}_7$, the d_{z^2} -derived band ($m^*/m_b \approx 5.5 \sim 8.3$) is also substantially more renormalized than its $d_{x^2-y^2}$ counterparts [22]. We note that a precise quantification for the γ band is complicated by hybridization effects and the opening of the density wave gap near E_F . Nevertheless, the enormous relative difference in renormalization is unambiguous. These results provide clear experimental evidence that electron correlations in $\text{Pr}_4\text{Ni}_3\text{O}_{10}$ are highly orbital-selective, being dramatically stronger for the d_{z^2} states than for the $d_{x^2-y^2}$ states.

DISENTANGLING THE DW-FOLDED ELECTRONIC STRUCTURE

In addition to the primary α and β bands and their superlattice-induced replicas, our μ -ARPES measurements reveal faint spectral weight along the $\bar{\Gamma} - \bar{Y}$ direction [highlighted by orange dashed circles in Fig. 2(b)]. This additional intensity appears exclusively near \bar{Y} and is absent around \bar{X} , indicating a pronounced in-plane anisotropy not observed in the bilayer analog [22]. Notably, a recent ARPES study of the isostructural compound $\text{La}_4\text{Ni}_3\text{O}_{10}$ recognized a small electron pocket (δ band) centered at the Γ' point [31], while it is different from the band features observed in $\text{Pr}_4\text{Ni}_3\text{O}_{10}$.

To resolve these fine features, the sample was reoriented to align with the electron analyzer slit direction. In this experimental geometry, the enhanced momentum resolution along the vertical cut allows previously obscured band features to be clearly resolved, as marked by red arrows in Figs. 3(a, b and d).

The high-resolution data reveals that the faint spectral weight is composed of multiple, distinct band crossings. Previous ARPES studies on $\text{La}_3\text{Ni}_2\text{O}_7$ have reported a small arc-like Fermi surface segment inside the β pocket, which have been attributed to either DW band folding orders [32] or impurity doping [22]. Our analysis reveals that these anisotropic features in $\text{Pr}_4\text{Ni}_3\text{O}_{10}$ align remarkably well with the dispersion of the main β band when translated in momentum space along the $\bar{\Gamma}-\bar{X}/\bar{Y}$ direction, as illustrated in Figs. 3(c, d). This implies that these additional bands originate from band-folding driven by charge or spin density wave vectors.

To validate this scenario, we quantitatively analyzed

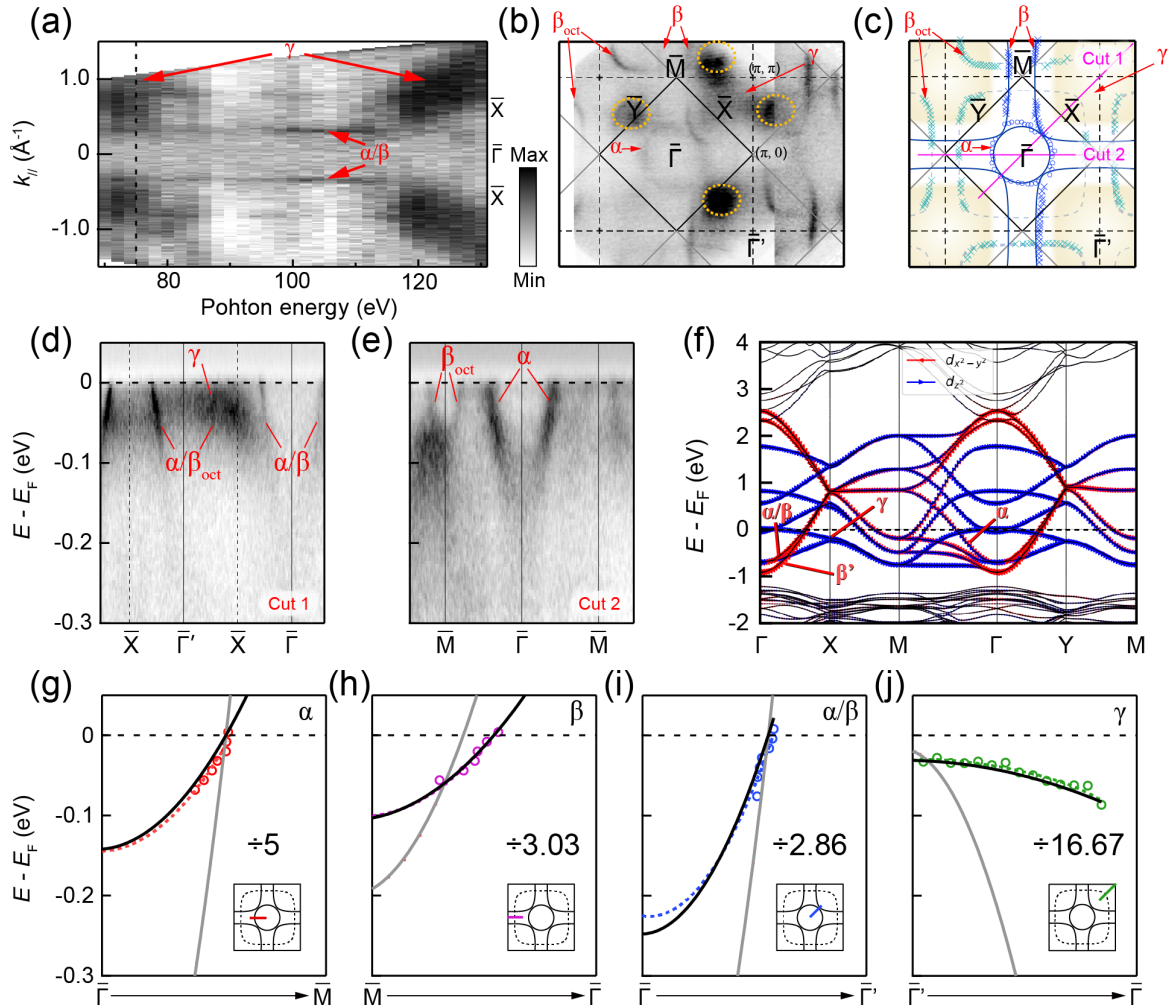


FIG. 2. (a) Photon energies- k_{\parallel} mapping along the $(0, 0)$ - (π, π) direction. It is obtained by integrating the spectral intensity within 50 meV with respect to the Fermi level; (b) Fermi surface mapping measured at 8 K by using synchrotron-based ARPES with a photon energy of 75 eV. It is obtained by integrating the spectral intensity within 50 meV with respect to the Fermi level. Brillouin zones are appended, with the dark solid lines represent the BZ of pristine lattice, and dark dash lines represent the BZ of octahedral lattice. (c) Measured Fermi surface of $\text{Pr}_4\text{Ni}_3\text{O}_{10}$ obtained from (b), appended with momentum cuts marks. It consists of two main Fermi surface sheets, α and β , and their octahedral back-folded bands α_{oct} and β_{oct} . (d-e) Band dispersions measured along momentum cuts Cut1 and Cut2, respectively. The location of the momentum cuts is shown in (c). The observed bands are labeled by their corresponding Fermi surface sheets; (f) DFT calculated band dispersion of $\text{Pr}_4\text{Ni}_3\text{O}_{10}$ without considering U. Red lines represent the contribution of Ni $3d_{x^2-y^2}$ orbitals and blue lines represent the contribution of Ni $3d_{z^2}$ orbitals. (g-j) Measured band dispersions (empty circles) and the corresponding calculated bands (solid lines). The direction of the corresponding momentum cut is shown in the inset at the bottom-right corner of each figure. The gray curve in the figure is the quadratic curve obtained by fitting the original DFT calculation results, while the black curve is the result after being scaled by the corresponding mass enhancement values to match the experimental data.

the momentum separation between the primary β band and these replicas [Figs. 3(e-g)]. Using the feature marked by red arrow 1 as an example, we tracked the peak positions in the momentum distribution curves (MDCs) near the Fermi level [Fig. 3(e)] and determined a scattering vector of $q_1 \approx 0.77 q_*$. This value is consistent with the reported incommensurate CDW wave vector measured by X-ray diffraction experiments, $q_{\text{cdw}} \approx 0.78 q_*$ [29]. A consistent analysis for the features marked by red arrows 2 and 3 [Fig. 3(b, d)] yields scattering vectors of ≈ 0.25 and $0.61 q_*$, which correspond to 1-

q_{cdw} and the SDW vector q_{sdw} of $\text{Pr}_4\text{Ni}_3\text{O}_{10}$, respectively [Figs. 3(f and g)]. More detailed analysis of those back-folded bands are presented in the Supplementary Information section II.

Taken together, this self-consistent analysis provides compelling evidence that the additional spectral features are not new intrinsic pockets (such as a δ band), but are rather replicas of the β band resulting from scattering by the primary CDW/SDW orders. As illustrated by the composite model in Fig. 3(h), the experimentally measured Fermi surface is excellently reproduced by su-

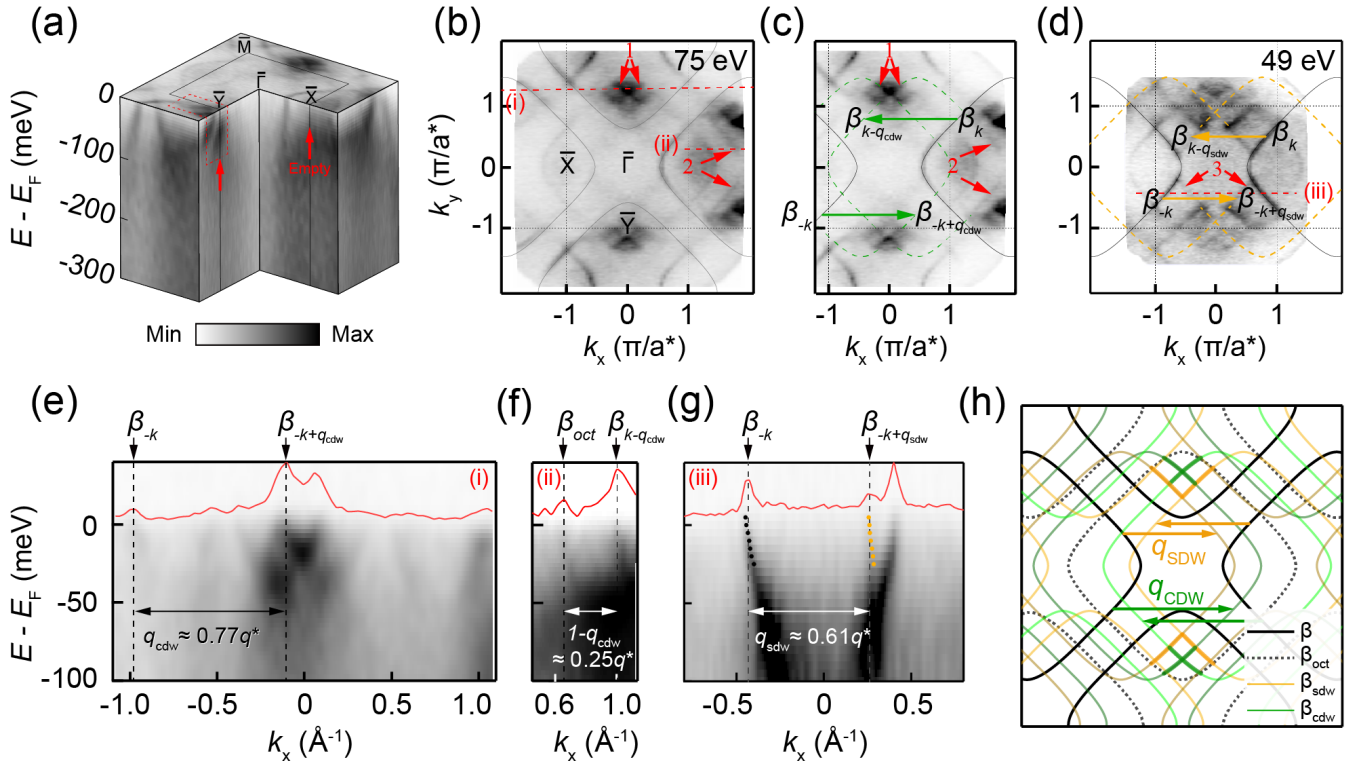


FIG. 3. (a) A 3D intensity plot of the ARPES spectra along orthogonal directions $\bar{\Gamma}$ - \bar{X} - \bar{Y} , with red arrows label the anisotropic features. (b) Fermi surface mapping measured at 8 K by using 75 eV photons, appended with β and β_{oct} pockets. It is obtained by integrating the spectral intensity within 10 meV with respect to the Fermi level. The $a^* = (a+b)/2$. The red arrows with label “1” mark the crossed extra features circled by β and β_{oct} pockets, and those labeled by “2” mark those extra features parallel to β_{oct} pockets. (c) Fermi surface mapping taken with 75 eV appended with β (dark solid frame) and β_{CDW} (green solid frame). (d) Fermi surface mapping measured at 8 K by using 49 eV photons, appended with β (dark solid frame) and β_{SDW} pockets (orange solid frame); (e) Band dispersions extracted from the 75 eV mapping along momentum cuts along $k_y = 0.775 \text{ \AA}^{-1}$ [cut (i), the inset of (e)]; (f) Band dispersions extracted from the 75 eV mapping along momentum cuts along $k_y = 0.205 \text{ \AA}^{-1}$ [cut (ii), the inset of (e)]; In (e-f) The MDC (red curve) extracted at Fermi level is appended on the top empty region above the E_F . The double-head arrows indicate the scattering vector; (g) Band dispersions extracted from the 49 eV mapping along momentum cuts along $k_y = -0.21 \text{ \AA}^{-1}$ (labeled by red dash line in the inset); (h) Schematic Fermi surface combined with all the pristine β (dark solid) and back-folded β result from octahedral tilting superlattice (dark dash lines), SDW (origin solid lines) and CDW (green solid lines).

perimposing the intrinsic bands with their replicas folded by the known SDW and CDW vectors. These results provide a comprehensive picture of the electronic structure in $\text{Pr}_4\text{Ni}_3\text{O}_{10}$, revealing that the complex Fermi surface topology is a direct consequence of coexisting spin and charge density wave orders and octahedra distortions.

DENSITY WAVE RELATED GAPS

Prior ARPES studies on trilayer nickelates reveal orbital- and momentum-selective DW reconstruction. Spectral features observed on the hole-like γ -band [23] and electron-like α -band [31] suggest a sheet-dependent coupling strength. Given the multi-sheet Fermi surface topology and unidirectional ordering vectors, it is crucial to identify which specific states are coupled by the ordering vector. Our comprehensive Fermi surface map-

ping enables a band-resolved analysis. At low temperatures, the γ -band top lies approximately 30 meV below the Fermi level and remains stationary across T_{DW} (Fig. S6). This finding contrasts with the band shifting reported in $\text{La}_4\text{Ni}_3\text{O}_{10}$ [23] but aligns with recent observations in $\text{La}_3\text{Ni}_2\text{O}_7$ [22], suggesting the γ band is not the primary location for the DW gap.

We next turned our attention to the electron-like α pocket around the zone center. At 8 K, well below T_{DW} , the spectral weight of the α band is significantly suppressed at E_F [Fig. 4(a)]. However, in the constant energy map taken at $E_F - 40$ meV [Fig. 4(b)], the α band becomes clearly resolved, indicative of a sizable density-wave gaps therein. By extracting the contours of the α pocket (red hollow circles) from this map and superimposing them onto the Fermi surface map [Fig. 4(c)], we observed that the α pocket coincides well with the

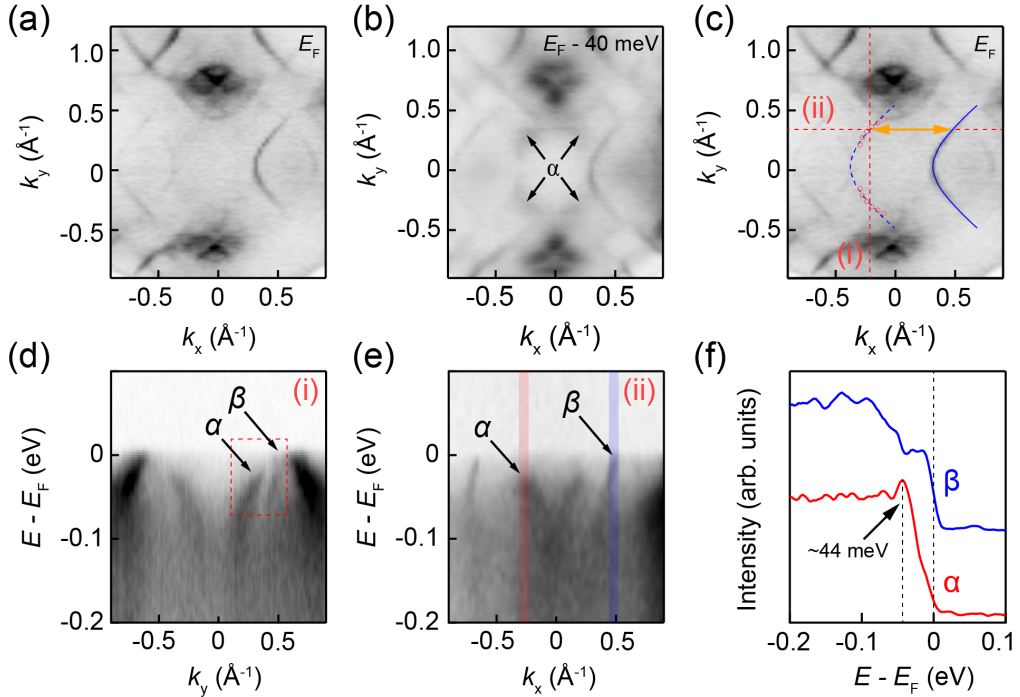


FIG. 4. (a) Fermi surface intensity map at E_F measured with 75 eV photons; (b) Constant energy map at $E_F - 30$ meV; black arrows indicate the α pocket. (c) The $E_F - 30$ meV map overlaid with the extracted α -band counter (hollow red circles) and the β -band counter (blue lines). The dashed red lines mark the momentum cut (i) and (ii) used in (d,e); the orange arrow highlights the nesting relation between the α and β pockets. (d,e) Energy-momentum dispersions along cut (i) and (ii), respectively. (f) The EDCs extracted from the shaded momentum windows in (e), taken at the α -band top (red) and at k_F of the β band (blue).

shifted β pocket ($\beta_{k-q_{sdw}}$). This geometric overlap provides strong evidence that Fermi surface nesting occurs between the α and β bands. Note that this finding is consistent with theoretical calculations, which suggest that the inter-orbital nesting dominates over intra-orbital contributions in driving the density-wave instability in trilayer nickelates [24, 33].

To quantitatively analyze the density-wave gap on the α band, we extracted band dispersion spectra [Figs. 4(d) and 4(e)] along the two orthorhombic directions cutting through the α pocket [marked as cuts (i) and (ii) in Fig. 4(c)], respectively. Both dispersions display pronounced back-bending for the α band, a characteristic feature of a DW-induced gap, whereas the β band shows much weaker modification. Quantitatively, based on the corresponding EDCs [Fig. 4(f)], we resolve a DW gap of approximately 44 meV in the α band. This magnitude is comparable to that observed by STM and optical spectroscopy in $\text{La}_4\text{Ni}_3\text{O}_{10}$ [14, 21]. Such orbital-selective gap can be well captured by the calculated band structure, as shown in SI section V. It is worth noting that the α band gap appears largely momentum independent, revealing a isotropic gap on α pocket, as shown in Fig. S5.

BAND SPLITTING OF THE β POCKETS

With the Fermi-surface complexity arising from lattice distortions and density-wave folding now fully characterized, another longstanding puzzle is why the trilayer system appears strikingly similar to its bilayer counterpart, despite the expectation that interlayer coupling within the trilayer block should induce a distinct bonding-antibonding splitting. In previous ARPES studies on $\text{La}_4\text{Ni}_3\text{O}_{10}$, this expected β -band splitting has never been resolved, and the absence was attributed to either limited experimental resolution or matrix-element suppression [23].

By rigorously distinguishing intrinsic features from the band-folding artifacts discussed above, we are now able to resolve this intrinsic splitting. As illustrated in Fig. 5(a), we identify two distinct regions (marked by red and blue dashed rectangular frames) where the β -band splitting is resolved using 75 eV and 49 eV photons, respectively. Fig. 5(b) displays an enlarged view of the Fermi surface within Region I. There, the β band is clearly split into two branches, denoted β and β' , and this splitting aligns well with DFT predictions for the bonding/antibonding states [Fig. 1(c)]. To better distinguish the split β band, we extract the band dispersion spectra [Figs. 5(d) and 5(e)] along the $\bar{\Gamma}-\bar{X}$ direction and along an off-high-

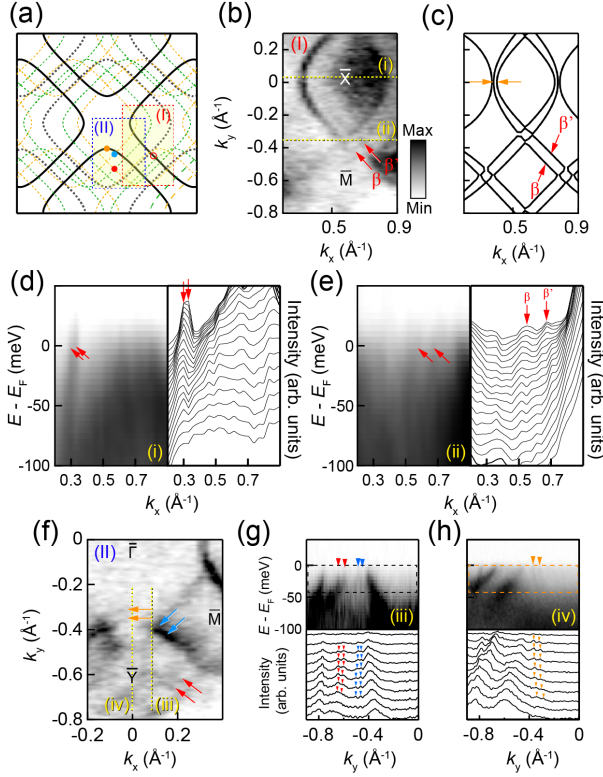


FIG. 5. (a) Schematic Fermi surface including all relevant bands. The red (blue) dashed box marks region I (II), corresponding to the zoomed Fermi-surface maps in (b) [(f)]. Colored dots indicate representative momenta k_β used for the splitting analysis in (e) and (g,h). (b) Zoomed Fermi-surface intensity map measured at 8 K with 75 eV photons. (c) Tight-binding Fermi surface calculated with an outer–outer NiO_2 -plane hopping $t_{\perp}^{x_{oo}} = 50$ meV. (d,e) Energy–momentum dispersions from the 75 eV dataset along the cuts $k_y = 0$ and $k_y = -0.38 \text{ \AA}^{-1}$, respectively, as indicated by the yellow dashed lines (i) and (ii) in (b); the corresponding MDC stacks are shown on the right. (f) Zoomed Fermi-surface intensity map measured at 8 K with 49 eV photons; arrows highlight the resolved β/β' splitting. (g,h) Energy-momentum dispersions from the 49 eV dataset along the cuts $k_x = 0$ and $k_x = 0.13 \text{ \AA}^{-1}$, respectively, as indicated by the yellow dashed lines (iii) and (iv) in (f). The accompanying MDCs (bottom panels) are integrated over the energy window from E_F to $E_F - 50$ meV. Inverted triangles mark the extracted band splittings.

symmetry direction at $k_y = -0.38 \text{ \AA}^{-1}$ [cuts (i) and (ii) in Fig. 5(b)], respectively. Along both directions, the β band splits into two distinct branches, with the MDCs confirming two well-defined peaks of comparable intensity. Crucially, the location of the β' branch does not coincide with any projection from our density-wave folding model [indicated by the red hollow circle in Fig. 5(a)], ruling out a CDW/SDW origin.

We also resolve distinct band splittings in Region II, specifically at the locations marked by red, blue and orange points in Fig. 5(a). Along the off-symmetry cut (iii) illustrated in Fig. 5(f), equivalent splitting features

are observed in the back-folded bands, β_{sdw} (blue arrows) and β_{cdw} (red arrows). The corresponding band dispersions and MDCs across these two bands are displayed in Fig. 5(g), where triangles highlight the positions of $\beta_{\text{sdw}/\text{cdw}}$ and their respective splittings. Surprisingly, along the high-symmetry $\bar{\Gamma}-\bar{Y}$ direction, the β band exhibits a sizable splitting, in clear contrast to the near degeneracy predicted by the DFT calculations shown in Fig. 1(c). This pronounced splitting is consistently observed both in the energy–momentum dispersion along this direction and in the corresponding MDCs, as highlighted by the orange triangles in Fig. 5(h). From a symmetry perspective, the $\bar{\Gamma}-\bar{Y}$ line is a high-symmetry direction along which the β band is composed purely of $d_{x^2-y^2}$ orbital character. Since interlayer coupling between $d_{x^2-y^2}$ orbitals is generally weak, one would expect the β bands to remain nearly degenerate along this direction. To identify the origin of the observed splitting, we constructed a tight-binding (TB) model (see Sec. V of the Supplemental Information). We find that interlayer hopping between the inner and outer layers alone, characterized by $t_{\perp}^{x_{io}}$, is insufficient to reproduce the observed splitting. In contrast, introducing an additional hopping term between the $d_{x^2-y^2}$ orbitals of the top and bottom Ni atoms, denoted $t_{\perp}^{x_{oo}}$, leads to a splitting at the same momentum location as seen in the ARPES measurements. A clearly resolvable splitting emerges only when $t_{\perp}^{x_{oo}}$ reaches approximately 50 meV, as indicated by the orange arrows in Fig. 5(c) and Fig. S8. These results point to unexpectedly complex interlayer hopping processes in trilayer nickelates, highlighting the need for further experimental and theoretical investigations.

SUMMARY

Our comprehensive μ -ARPES investigation establishes a coherent picture of how trilayer coupling, octahedral distortions, and intertwined DW orders cooperate to shape the low-energy electronic structure of $\text{Pr}_4\text{Ni}_3\text{O}_{10}$. By selecting a single structural/DW domain, we eliminate the spectral averaging that obscured prior ARPES studies of RP nickelates, allowing us to explicitly separate intrinsic dispersions from folding artifacts. This enables (i) a domain-resolved identification of SDW- and CDW-induced back-folded bands with distinct incommensurate vectors; in light of recent transport evidence suggesting a close connection between SDW order and superconductivity in the RP nickelate family [11, 13, 34], our results highlight the importance of explicitly accounting for SDW domain selectivity in future electronic-structure studies; (ii) a momentum-resolved determination of the dominant regions for DW gap formation, which validating the existence of the gap in momentum space and identifying inter-orbital nesting as the primary driver of the SDW instability; and (iii) the direct resolution of the

long-sought intrinsic trilayer β -band splitting and discovery of inter-layer hopping between the outmost Ni-O layers. Together, these findings provides a solid foundation for modeling the interplay density waves instability and electronic structures in trilayer nickelate superconductors.

ACKNOWLEDGMENT

This work is supported by National Natural Science Foundation of China (Grants No.12494593, No.12504079), National Key R&D Program of China (Grants No. 2024YFA1408103, No. 2023YFA1406304), Innovation Program for Quantum Science and Technology (Grant No. 2021ZD0302803), and New Cornerstone Science Foundation. Z.C.J. acknowledges the China National Postdoctoral Program for Innovative Talents (BX20240348) and Xiaomi Young Talents Program. D.W.S. acknowledges the Anhui Provincial Natural Science Foundation (Grant No. 2408085J003). We thank the Shanghai Synchrotron Radiation Facility (SSRF) for the beamtime on beamline 03U (31124.02.SSRF.BL03U), which is supported by ME² project under contract No. 11227902 from National Natural Science Foundation of China.

AUTHOR CONTRIBUTION

D.W.S. and D.L.F. proposed and designed the research. E.K.Z. and J.Z. contributed to single crystal growth and characterizations. Y.X.W and K.J. contributed to the DFT band calculations. Z.C.J., R.F.Z. and Y.H. carried out the ARPES experiments. Z.C.J., Z.T.L., J.S.L., R.F.Z., W.C.J., Y.H., Q.J., M.Y., D.W.S. contributed to the development and maintenance of ARPES system and beamline. Z.C.J., E.K.Z., Y.X.Z., Z.T.L., X.N.Z. and D.W.S. analyzed the data. Z.C.J., Z.T.L., Y.X.W., K. J. D.W.S. and D.L.F. wrote the manuscript. All authors participated in the discussion and comment on the paper.

METHODS

A. Sample growth and characterization

Precursor powder of $\text{Pr}_4\text{Ni}_3\text{O}_{10}$ was prepared by a standard solid-state reaction. Stoichiometric cation ratios corresponding to $\text{Pr}_4\text{Ni}_3\text{O}_{10}$ were obtained by mixing Pr_6O_{11} (Aladdin, 99.99 %) and NiO (Aladdin, 99.99 %). The powders were thoroughly ground and mixed, then calcined at 1373 K three times to ensure a complete and homogeneous reaction. An additional 0.5 % NiO was added to compensate for possible volatilization

during crystal growth. Subsequently, the reacted powder was isostatically pressed into 12 cm-long, 6 mm-diameter rods and sintered in air at 1673 K for 12 h. Single crystals were grown in a vertical optical floating-zone furnace (Model HKZ, SciDre) via a two-step procedure: first, the rod was rapidly scanned (20 mm h^{-1} , 10 bar O_2) to enhance density; then growth was carried out at 2 mm h^{-1} under 130–150 bar O_2 .

Transport measurements were performed in a Quantum Design PPMS (1.8–300 K) using a standard four-probe method. Gold pads were deposited on the sample first to ensure stable connections during measurement.

B. ARPES Measurements

Synchrotron-based ARPES measurements were carried out at the BL03U endstation of the Shanghai Synchrotron Radiation Facility (SSRF), using a Scienta DA30 electron analyzer with vertical slit of 300 μm (perpendicular to the laboratory floor). The base pressure during measurements was lower than 8×10^{-11} Torr. All Samples were cleaved *in situ* below 10 K at in the measurement chamber. The measurement temperature was maintained at 8 K unless otherwise specified in the main text. A focused beam spot smaller than 15 \times 15 μm^2 was adopted during the measurements. The measurements were mainly performed with photon energies of 49 and 75 eV with linear horizontal (LH) light (parallel to the laboratory floor). The overall energy resolution was \sim 10 meV and angular resolution was \sim 0.3°.

C. Calculations

Our DFT calculations employ the Vienna ab-initio simulation package (VASP) code [35] with the projector augmented wave (PAW) method [36]. The exchange-correlation functional employs the SCAN functional [37], a type of meta-GGA approach that offers higher accuracy than traditional GGA functionals. The cutoff energy for expanding the wave functions into a plane-wave basis is set to be 500 eV. The energy convergence criterion is 10^{-8} eV. All calculations are conducted using the primitive cell. The Γ -centered $9 \times 9 \times 4$ k-meshes are used. When calculating the Fermi surface, first apply the Wannier90 software [38] to fit the DFT-calculated bands, then use the generated hr file to compute the Fermi surface. Directly modifying the hopping parameters in the hr file allows for obtaining Fermi surfaces under different parameters.

* Equal contributions

[†] liuzt@sari.ac.cn
[‡] jiangkun@iphy.ac.cn
[§] zhaoj@fudan.edu.cn
[¶] dwshen@ustc.edu.cn
^{**} dlfeng@ustc.edu.cn

[1] Armitage, N., Fournier, P. & Greene, R. Progress and perspectives on electron-doped cuprates. *Reviews of Modern Physics* **82**, 2421–2487 (2010).

[2] Dai, P. Antiferromagnetic order and spin dynamics in iron-based superconductors. *Reviews of Modern Physics* **87**, 855–896 (2015).

[3] Chang, J. *et al.* Direct observation of competition between superconductivity and charge density wave order in $\text{YBa}_2\text{Cu}_3\text{O}_{6.67}$. *Nature Physics* **8**, 871–876 (2012).

[4] Sun, H. *et al.* Signatures of superconductivity near 80 k in a nickelate under high pressure. *Nature* **621**, 493–498 (2023).

[5] Zhu, Y. *et al.* Superconductivity in pressurized trilayer $\text{La}_4\text{Ni}_3\text{O}_{10-\delta}$ single crystals. *Nature* **631**, 531–536 (2024).

[6] Zhang, Y. *et al.* High-temperature superconductivity with zero resistance and strange-metal behaviour in $\text{La}_3\text{Ni}_2\text{O}_{7-\delta}$. *Nature Physics* **20**, 1269–1273 (2024).

[7] Wang, N. *et al.* Bulk high-temperature superconductivity in pressurized tetragonal $\text{La}_2\text{PrNi}_2\text{O}_7$. *Nature* **634**, 579–584 (2024).

[8] Ko, E. K. *et al.* Signatures of ambient pressure superconductivity in thin film $\text{La}_3\text{Ni}_2\text{O}_7$. *Nature* **638**, 935–940 (2025).

[9] Zhou, G. *et al.* Ambient-pressure superconductivity onset above 40 K in $(\text{La}, \text{Pr})_3\text{Ni}_2\text{O}_7$ films. *Nature* **640**, 641–646 (2025).

[10] Zhang, E. *et al.* Bulk superconductivity in pressurized trilayer nickelate $\text{Pr}_4\text{Ni}_3\text{O}_{10}$ single crystals. *Physical Review X* **15**, 021008 (2025).

[11] Shi, M. *et al.* Pressure induced superconductivity in hybrid Ruddlesden-Popper $\text{La}_5\text{Ni}_3\text{O}_{11}$ single crystals. *Nature Physics* 1–7 (2025).

[12] Wang, G. *et al.* Pressure-induced superconductivity in polycrystalline $\text{La}_3\text{Ni}_2\text{O}_{7-\delta}$. *Physical Review X* **14**, 011040 (2024).

[13] Zhao, D. *et al.* Pressure-enhanced spin-density-wave transition in double-layer nickelate $\text{La}_3\text{Ni}_2\text{O}_{7-\delta}$. *Science Bulletin* (2025).

[14] Xu, S. *et al.* Collapse of density wave and emergence of superconductivity in pressurized- $\text{La}_4\text{Ni}_3\text{O}_{10}$ evidenced by ultrafast spectroscopy. *Nature Communications* **16**, 7039 (2025).

[15] Dong, Z. *et al.* Visualization of oxygen vacancies and self-doped ligand holes in $\text{La}_3\text{Ni}_2\text{O}_{7-\delta}$. *Nature* **630**, 847–852 (2024).

[16] Dong, Z. *et al.* Interstitial oxygen order and its competition with superconductivity in $\text{La}_2\text{PrNi}_2\text{O}_{7+\delta}$. *Nature Materials* 1–8 (2025).

[17] Puphal, P. *et al.* Unconventional crystal structure of the high-pressure superconductor $\text{La}_3\text{Ni}_2\text{O}_7$. *Physical Review Letters* **133**, 146002 (2024).

[18] Chen, X. *et al.* Polymorphism in the ruddlesden–popper nickelate $\text{La}_3\text{Ni}_2\text{O}_7$: discovery of a hidden phase with distinctive layer stacking. *Journal of the American Chemical Society* **146**, 3640–3645 (2024).

[19] Zhou, X. *et al.* Revealing nanoscale structural phase separation in $\text{La}_3\text{Ni}_2\text{O}_{7-\delta}$ single crystal via scanning near-field optical microscopy. *arXiv e-prints* arXiv:2410.06602 (2024).

[20] Gupta, N. K. *et al.* Anisotropic spin stripe domains in bilayer $\text{La}_3\text{Ni}_2\text{O}_7$. *Nature Communications* **16**, 6560 (2025).

[21] Li, M. *et al.* Direct visualization of an incommensurate unidirectional charge density wave in $\text{La}_4\text{Ni}_3\text{O}_{10}$. *Physical Review B* **112**, 045132 (2025).

[22] Yang, J. *et al.* Orbital-dependent electron correlation in double-layer nickelate $\text{La}_3\text{Ni}_2\text{O}_7$. *Nature Communications* **15**, 4373 (2024).

[23] Li, H. *et al.* Fermiology and electron dynamics of trilayer nickelate $\text{La}_4\text{Ni}_3\text{O}_{10}$. *Nature communications* **8**, 704 (2017).

[24] Jia, X. *et al.* Lattice-charge coupling in a trilayer nickelate with intertwined density wave order. *arXiv preprint arXiv:2507.13513* (2025).

[25] Jiang, K., Wang, Z. & Zhang, F.-C. High-temperature superconductivity in $\text{La}_3\text{Ni}_2\text{O}_7$. *Chinese Physics Letters* **41**, 017402 (2024).

[26] Chen, C.-Q., Luo, Z., Wang, M., Wú, W. & Yao, D.-X. Trilayer multiorbital models of $\text{La}_4\text{Ni}_3\text{O}_{10}$. *Physical Review B* **110**, 014503 (2024).

[27] Yang, Q.-G., Jiang, K.-Y., Wang, D., Lu, H.-Y. & Wang, Q.-H. Effective model and $s\pm$ -wave superconductivity in trilayer nickelate $\text{La}_4\text{Ni}_3\text{O}_{10}$. *Physical Review B* **109**, L220506 (2024).

[28] Tian, P.-F., Ma, H.-T., Ming, X., Zheng, X.-J. & Li, H. Effective model and electron correlations in trilayer nickelate superconductor $\text{La}_4\text{Ni}_3\text{O}_{10}$. *Journal of Physics: Condensed Matter* **36**, 355602 (2024).

[29] Samarakoon, A. M. *et al.* Bootstrapped dimensional crossover of a spin density wave. *Physical Review X* **13**, 041018 (2023).

[30] Zhou, X. *et al.* Revealing nanoscale structural phase separation in $\text{La}_3\text{Ni}_2\text{O}_{7-\delta}$ single crystal via scanning near-field optical microscopy. *arXiv preprint arXiv:2410.06602* (2024).

[31] Du, X. *et al.* Dichotomy in low-and high-energy band renormalizations in trilayer nickelate $\text{La}_4\text{Ni}_3\text{O}_{10}$: A comparison with cuprates. *Physical Review Letters* **135**, 146506 (2025).

[32] Au-Yeung, C. C. *et al.* Universal electronic structure of layered nickelates via oxygen-centered planar orbitals. *arXiv preprint arXiv:2502.20450* (2025).

[33] Zhang, J. *et al.* Intertwined density waves in a metallic nickelate. *Nature communications* **11**, 6003 (2020).

[34] Shi, M. *et al.* Absence of superconductivity and density-wave transition in ambient-pressure tetragonal $\text{La}_4\text{Ni}_3\text{O}_{10}$. *Nature Communications* **16**, 2887 (2025).

[35] Kresse, G. & Furthmüller, J. Efficient iterative schemes for ab initio total-energy calculations using a plane-wave basis set. *Phys. Rev. B* **54**, 11169–11186 (1996). URL <https://link.aps.org/doi/10.1103/PhysRevB.54.11169>.

[36] Kresse, G. & Joubert, D. From ultrasoft pseudopotentials to the projector augmented-wave method. *Phys. Rev. B* **59**, 1758–1775 (1999).

[37] Sun, J., Ruzsinszky, A. & Perdew, J. P. Strongly constrained and appropriately normed semilocal density functional. *Phys. Rev. Lett.* **115**, 036402 (2015). URL <https://link.aps.org/doi/10.1103/PhysRevLett.115.036402>.

[38] Pizzi, G. *et al.* Wannier90 as a community code: new features and applications. *J. Phys. Condens. Matter*.

32, 165902 (2020). URL <https://doi.org/10.1088/1361-648X/ab51ff>.